nature nanotechnology

LETTERS

PUBLISHED ONLINE: 3 APRIL 2011 | DOI: 10.1038/NNANO.2011.39

Nanoscale Joule heating, Peltier cooling and current crowding at graphene–metal contacts

Kyle L. Grosse[1,2], Myung-Ho Bae[2,3], Feifei Lian[2,3], Eric Pop[2,3,4]* and William P. King[1,2,4,5]*

The performance and scaling of graphene-based electronics[1] is limited by the quality of contacts between the graphene and metal electrodes[2–4]. However, the nature of graphene–metal contacts remains incompletely understood. Here, we use atomic force microscopy to measure the temperature distributions at the contacts of working graphene transistors with a spatial resolution of ~10 nm (refs 5–8), allowing us to identify the presence of Joule heating[9–11], current crowding[12–16] and thermoelectric heating and cooling[17]. Comparison with simulation enables extraction of the contact resistivity (150–200 Ω μm^2) and transfer length (0.2–0.5 μm) in our devices; these generally limit performance and must be minimized. Our data indicate that thermoelectric effects account for up to one-third of the contact temperature changes, and that current crowding accounts for most of the remainder. Modelling predicts that the role of current crowding will diminish and the role of thermoelectric effects will increase as contacts improve.

The physical phenomena primarily responsible for changes in the temperature of semiconductor devices during electrical operation are the Joule and Peltier effects. The Joule effect[9] occurs as charge carriers dissipate energy within the lattice, and is proportional to resistance and the square of the current. The Peltier effect[17] is proportional to the magnitude of the current through and the difference in thermopower at a junction of dissimilar materials, leading to either heating or cooling depending on the direction of current flow. A rise in temperature negatively affects electronic devices, decreasing performance by lowering carrier mobility[10] and reducing the device lifetime[18].

Joule heating in graphene transistors results in a local temperature rise ('hot spot')[11,19]; the position of this corresponds to the carrier density minimum and its shape has been linked to the density of states[11]. In contrast, thermal phenomena at graphene–metal contacts are not well understood, although thermoelectric effects play a role at monolayer–bilayer interfaces[20]. Given that the thermopower of graphene can reach $S \approx 100\ \mu V\ K^{-1}$ slightly above room temperature[21–23], Peltier contact effects could be significant in future graphene electronics under normal operating conditions. Moreover, little is known about transport at graphene contacts, although they are clearly recognized as a fundamental roadblock for graphene nanoelectronics[2–4].

Here, we use atomic force microscopy (AFM)-based temperature measurements[5–8] with a spatial resolution of ~10 nm and temperature resolution of ~250 mK, combined with detailed simulations, to uncover not only the effects of Joule heating, but also to reveal Peltier cooling and current crowding at graphene–metal contacts. These effects are key to understanding the scalability and ultimate performance of future graphene electronics. Figure 1 presents a typical two-terminal, backgated monolayer graphene device fabricated as detailed in the Methods. The colour overlay in Fig. 1 indicates the measured temperature rise (additional details of the measurement technique are described in the Methods and Supplementary Information).

To understand transport in the graphene device we built upon our previous models that include Joule heating and electrostatics[10,11], here incorporating current crowding and thermoelectric effects at the contacts. Current crowding occurs as the current transfers between the graphene and the metal contact over a finite length, leading to a non-uniform current density that is higher at the edge of the metal contact and decreases to zero deeper into the contact (Fig. 3, inset). The effect is well-known in carbon-nanotube[12–14] and silicon devices[15,16]. The contact transfer length $L_T = (\rho_C/R_S)^{1/2}$ is the distance over which $1/e$ of the current is transferred to the metal contact, where R_S is the sheet resistance of graphene[10,11] and ρ_C is the interface resistivity. The macroscopic contact resistance is therefore $R_C = \rho_C/(WL_T)\coth(L_C/L_T)$, where L_C is the physical electrode contact length over the graphene[15,16]. The current crowding effect generates resistive heating along the graphene–metal contact, as explored below. The thermoelectric effect at the graphene–metal interface can result in heating or cooling along the contacts, depending on the direction of current

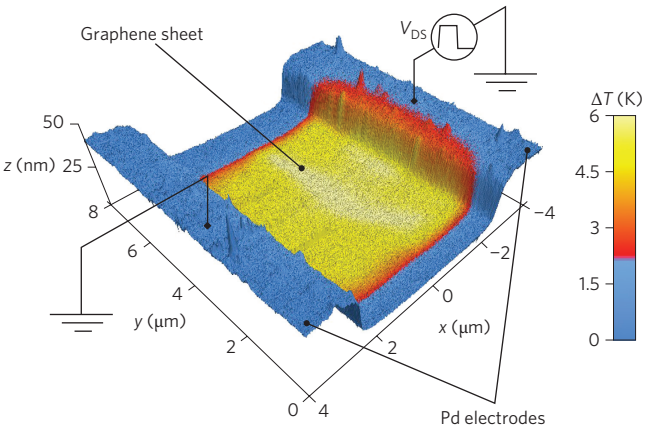

Figure 1 | Device layout. The temperature of the graphene device during device operation is overlaid on the topography. The device was biased with backgate voltage $V_G = 0$ V, and square-wave input $V_{DS} = 1.5$ V at 65 kHz and 50% duty (power, ~1.5 mW). Colder edges are consistent with heat sinking and higher edge carrier concentration[30,31] owing to fringing heat and electric field effects.

[1]Department of Mechanical Science and Engineering, University of Illinois Urbana-Champaign, Urbana, Illinois 61801, USA, [2]Micro and Nanotechnology Laboratory, University of Illinois Urbana-Champaign, Urbana, Illinois 61801, USA, [3]Department of Electrical and Computer Engineering, University of Illinois Urbana-Champaign, Urbana, Illinois 61801, USA, [4]Beckman Institute for Advanced Studies, University of Illinois Urbana-Champaign, Urbana, Illinois 61801, USA, [5]Department of Materials Science and Engineering, University of Illinois Urbana-Champaign, Urbana, Illinois 61801, USA. *e-mail: epop@illinois.edu; wpk@illinois.edu

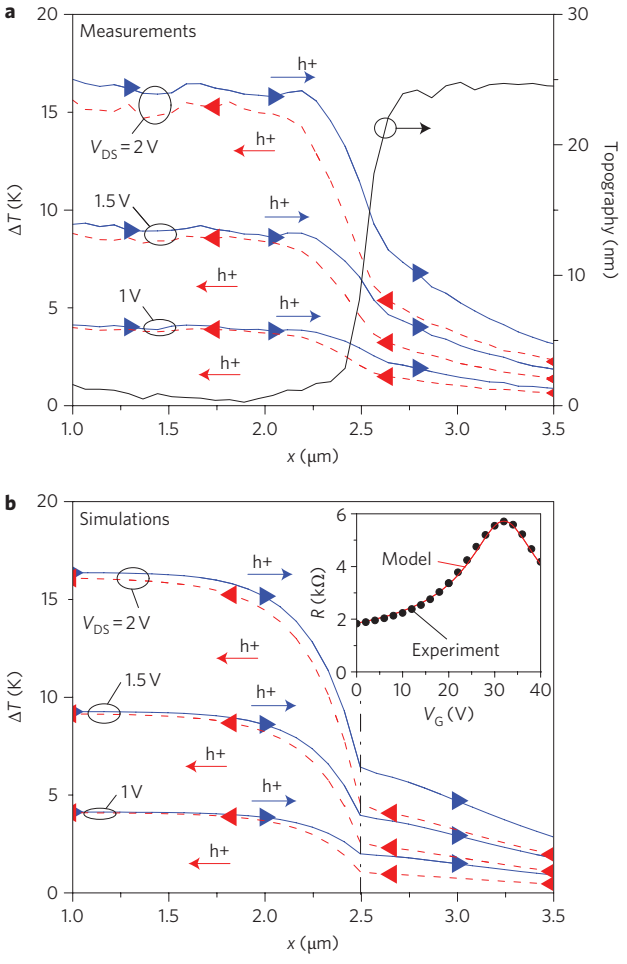

Figure 2 | Measured and predicted contact heating and cooling. **a**,**b**, Measured (**a**) and simulated (**b**) temperature profiles at the graphene–metal contact for a device with hole flow into (right arrows) and out of (left arrows) the contact. Operation is at $V_G = 0$ V (Dirac voltage, $V_0 = 32$ V) and $V_{DS} = 1$, 1.5 and 2 V, both forward and reverse. Device dimensions are $L = 5$ μm, $W = 4$ μm, $L_C = 5$ μm, and the edge of the graphene–palladium contact is at $x = 2.5$ μm. Inset to **b**: resistance (R) including contacts versus V_G for both experiment (symbols) and the model (line) used to fit the device mobility.

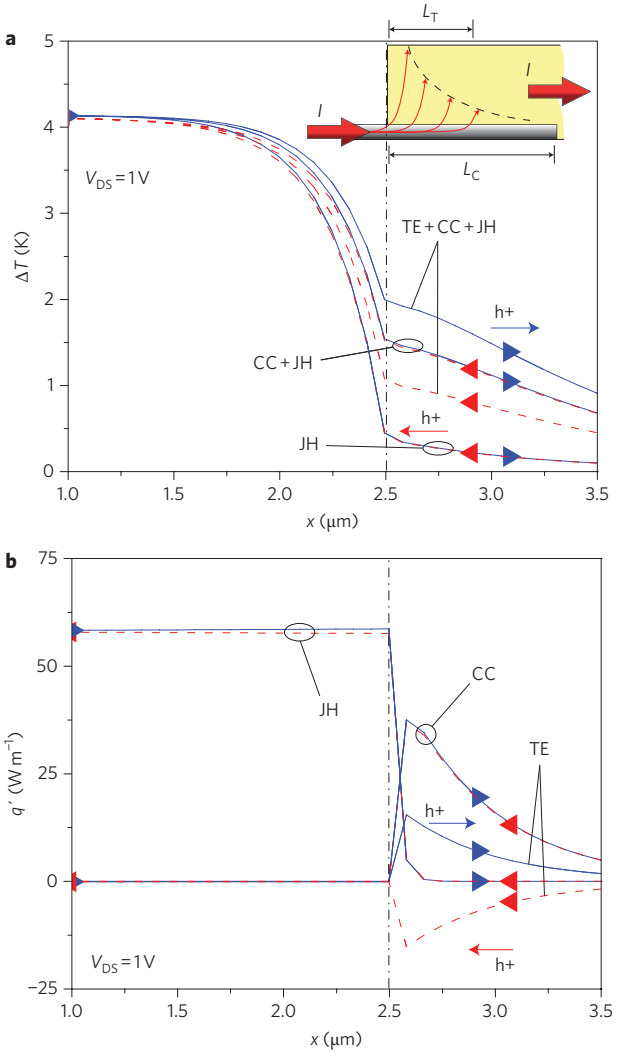

Figure 3 | Relative contribution of contact effects. **a**, Simulations showing relative contributions of Joule heating (JH), current crowding (CC) and the thermoelectric (TE) effect to the temperature distribution at the graphene–palladium contact at $V_{DS} = 1$ V and $V_G = 0$ V. Including current crowding ('CC + JH') leads to a more gradual temperature decrease than that of the Joule heating model alone, and adding in the thermoelectric term introduces heating and cooling that depends on current flow direction. All three components are necessary to match the experimental data in Fig. 2. Inset: schematic of current crowding at the graphene–metal contact (not to scale). **b**, Heat generation per unit length (q') as a function of position along the device. The separate contributions of Joule heating, current crowding and the thermoelectric effect to heat generation near the contact are shown. Joule heating dominates in the graphene sheet. In the contact, current crowding accounts for ~two-thirds and the thermoelectric effect for ~one-third of the temperature change, with the present parameters.

flow and the sign of the Seebeck coefficient S. Here, S is calculated at each point along the metal–graphene contacts self-consistently with the charge density, potential and contact temperature (details of current crowding and thermoelectric implementation are described in the Supplementary Information).

Figure 2 compares the measured temperature increase profiles with simulations for a device with $V_{DS} = 1$, 1.5 and 2 V, under both forward and reverse current flow. Fitting low-field measurements (Fig. 2b, inset) yields mobility $\mu \approx 3{,}230$ cm^2 V^{-1} s^{-1} and minimum carrier density $n_0 \approx 1.8 \times 10^{11}$ cm^{-2} for this device, consistent with the results of other studies[10,11,24]. We set $V_G = 0$ V in Fig. 2, corresponding to a hole concentration $p \approx 2.3 \times 10^{12}$ cm^{-2}. Joule heating is evidently dominant in the graphene sheet itself[11], showing a temperature rise that scales with the square of the applied voltage. However, the temperature profile within the metal contact is higher when holes are flowing from graphene into the contact, indicating a clear thermoelectric effect, as discussed below. The three families of curves in Fig. 2b were generated taking into account all contact effects (Joule heating + current crowding + thermoelectric), and are in excellent agreement with the experimental temperatures from Fig. 2a. Interestingly, we note that the temperature changes at the contact are not strongly dependent on the in-plane thermal conductivity of graphene, because most heat dissipation occurs 'vertically' into the SiO_2 and (once inside the metal contacts) into the palladium electrode. Our choices for the material thermal properties and the associated uncertainties are described in the Supplementary Information.

Only one independent fitting parameter is needed to match all experimental temperature profiles for a given contact, here $\rho_C \approx 150\ \Omega\ \mu m^2$. (See Supplementary Information for an analysis of a second device.) This enables direct extraction of the transfer length, which changes with gate bias, $L_T \approx 430$–200 nm for $V_G = 0$ to $V_0 = 32$ V. The contact resistance per width is

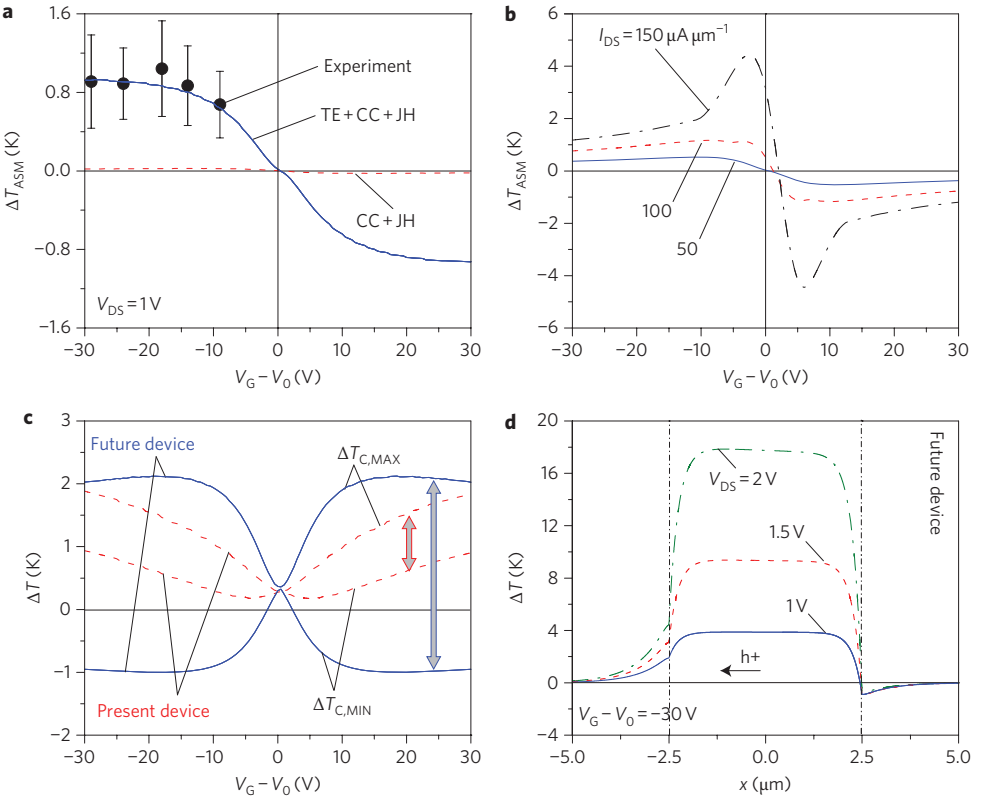

Figure 4 | Contact temperature under varying conditions. a, Comparison of predicted and measured temperature asymmetry ΔT_{ASM} at $V_{DS} = 1$ V. ΔT_{ASM} is the maximum difference in temperature rise of the contact for forward and reverse current flows (Supplementary Fig. S6). Joule heating and current crowding effects are negligible, and the thermoelectric effect dominates the temperature asymmetry and can be used to extract the Seebeck coefficient (see main text and Supplementary Information). **b**, Predictions of ΔT_{ASM} as a function of current density. **c**, Contact temperature rise for the present device ($\rho_C = 150\ \Omega\ \mu m^2$, $\mu = 3{,}230\ cm^2\ V^{-1}\ s^{-1}$) and a future device with greatly improved contact resistance and mobility ($\rho_C = 1\ \Omega\ \mu m^2$, $\mu = 2 \times 10^4\ cm^2\ V^{-1}\ s^{-1}$) at $V_{DS} = 1$ V. The maximum and minimum temperature rises at the contacts are indicated by $\Delta T_{C,MAX}$ and $\Delta T_{C,MIN}$, and the gap between the two curves is ΔT_{ASM}, shown by the arrows. The temperature changes owing to the thermoelectric effect at the contacts are enhanced in future devices. **d**, Projected temperature profile along the channel of a 5-μm-long device with the improved parameters. Note the negative temperature change at the right contact, where the current crowding is now negligible and the thermoelectric cooling becomes dominant.

$R_C W \approx 350$–$750\ \Omega\ \mu m$ over this range, about a factor of two lower for our thin chromium (0.5 nm)/palladium contacts than previous reports (which used thicker chromium (15 nm)/gold, titanium (10 nm)/gold, or nickel[2,3]). Nevertheless, the relatively large L_T has profound consequences for device scaling, as contact length $L_C > L_T$ (on the order of ~1 μm) must be chosen to minimize R_C in sub-100 nm graphene devices. The size of the contacts would therefore dwarf the size of the channel itself. In comparison, the typical contact resistance of modern silicon devices is ~100 Ω μm, achieved with contacts of <100 nm (refs 25,26).

Figure 3a shows temperature rise predictions including only Joule heating, then adding in current crowding and then the thermoelectric effect. When only Joule heating is considered, there is a sharp temperature drop in the electrode, which acts as a heat sink. The current crowding term introduces additional heating into the electrode. Finally, the inclusion of the thermoelectric effect generates a temperature asymmetry (heating versus cooling) with respect to carrier flow direction. The thermoelectric effect is evident as a difference in temperature when the current flow is reversed, shown in Figs 2 and 3. At $V_{DS} = 1$ V, the thermoelectric effect cools one electrode by ~0.5 K (~30%) under carrier outflow, and heats the opposite electrode similarly under carrier inflow. To understand the individual contributions of Joule heating, current crowding and the thermoelectric effect within the contact, Fig. 3b shows their separate heat generation rates, with the thermoelectric effect less than zero under hole flow from contact to graphene.

Figure 4 further explores how the thermoelectric effect affects temperature rise within the contact. Here, we define the temperature asymmetry as $\Delta T_{ASM} = \Delta T(j+) - \Delta T(j-)$, the maximum difference in temperature rise between the two current flow directions (Supplementary Fig. S6). Figure 4a compares ΔT_{ASM} for a simulation to experimental results at $V_{DS} = 1$ V, again highlighting the dominant role played by the thermoelectric effect. ΔT_{ASM} changes sign when the gate voltage is swept through V_0, as the sign of the graphene thermopower changes when majority carriers switch from holes to electrons[20–23]. Joule heating and current crowding effects make insignificant contributions to the temperature asymmetry when the local graphene sheet resistance (R_S) changes with gate bias. (See Supplementary movie for further illustration of these transitions.) In addition, a comparison of our simulations with the temperature data from Fig. 4a allows an independent extraction of the thermopower ($S \approx 63\ \mu V\ K^{-1}$ at $V_G - V_0 = -25$ V), which is in good agreement with previous values measured for monolayer graphene (see Supplementary Information)[22,23]. Figure 4b presents the temperature asymmetry with respect to current flow, indicating that at intermediate current density it can reach several degrees kelvin. Such temperature changes can affect long-term device reliability[18], and could be even more important in submicrometre graphene devices, which are essentially dominated by their contacts.

The panels in Fig. 4c,d examine the absolute temperature rise at the contacts in improved future graphene devices, for which we

expect higher mobility and reduced contact resistivity. The 'present device' uses the simulation parameters fit to the experiments at hand. The 'future projection' assumes a desirable 'good performance' on SiO_2 of $\mu = 2 \times 10^4$ cm^2 V^{-1} s^{-1} and $\rho_C = 1\,\Omega\,\mu$m^2. We find that such improvements in device quality tend to enhance thermoelectric contact asymmetry. The increase in mobility and decrease in contact resistivity both lead to a shorter transfer length L_T, and enhancement of the electric field at the contact. This, in turn, leads to an increase in the temperature and potential gradient (field), enhancing the thermoelectric effect at the contacts.

In summary, we have used an AFM thermal imaging technique to observe temperature distributions at graphene–metal contacts with unprecedented spatial and temperature resolution. The observed temperature distributions can be explained only with a significant thermoelectric effect, combined with current crowding and Joule heating. Projections based on simulations fit to our initial experiments suggest that, with technology scaling and improvement, the roles of contact resistance and current crowding will diminish, whereas the role of thermoelectric contact effects will become more significant for future graphene nanoelectronics.

Methods

Sample fabrication. Graphene was mechanically exfoliated[10,11] on 300 nm thermal SiO_2 with highly n-doped silicon as the backgate. Samples were annealed in a chemical vapour deposition chamber with argon/hydrogen at 400 °C for 35 min before and after graphene deposition[27]. Electron-beam lithography was used to pattern the electrodes and shape the graphene sheets. Chromium/palladium (0.5 nm/40 nm) source and drain electrodes were evaporated, followed by an oxygen plasma etch to define the device shape. Single-layer graphene was confirmed with Raman spectroscopy[28,29], and electrode thickness was verified by AFM scan. For thermal AFM measurements, a 65 nm layer of poly(methyl methacrylate) (PMMA) was spun onto the device[8], with the thickness confirmed by ellipsometry. The PMMA served to amplify the thermal signal for the AFM temperature measurements, and to protect the samples from spurious doping effects during measurements. Complete data for two devices are presented in detail here and in the Supplementary Information, from a total of six devices tested, all of which yielded similar results.

Thermal AFM measurement. Scanning Joule expansion microscopy (SJEM)[5–8] was used to measure the temperature rise during device operation. Device heating was induced with a 65 kHz, 50% duty square wave with amplitude V_{DS}. Thermomechanical expansion of the sample was measured by monitoring the cantilever deflection signal with a lock-in amplifier technique. Each temperature profile shown was averaged over 128 line scans, each 3 μm long, across the graphene–electrode junction. The measurement could be improved with longer scans, but was limited here to avoid Dirac voltage shift under prolonged electrical stress. Additional details regarding setup and calibration of the SJEM experiment are available in the Supplementary Information.

Received 27 January 2011; accepted 24 February 2011; published online 3 April 2011

References

1. Schwierz, F. Graphene transistors. *Nature Nanotech.* **5,** 487–496 (2010).
2. Nagashio, K., Nishimura, T., Kita, K. & Toriumi, A. Systematic investigation of the intrinsic channel properties and contact resistance of monolayer and multilayer graphene field-effect transistor. *Jpn J. Appl. Phys.* **49,** 051304 (2010).
3. Nagashio, K., Nishimura, T., Kita, K. & Toriumi, A. Contact resistivity and current flow path at metal/graphene contact. *Appl. Phys. Lett.* **97,** 143514 (2010).
4. Khomyakov, P. A., Starikov, A. A., Brocks, G. & Kelly, P. J. Nonlinear screening of charges induced in graphene by metal contacts. *Phys. Rev. B* **82,** 115437 (2010).
5. Varesi, J. & Majumdar, A. Scanning Joule expansion microscopy at nanometer scales. *Appl. Phys. Lett.* **72,** 37–39 (1998).
6. Majumdar, A. & Varesi, J. Nanoscale temperature distributions measured by scanning Joule expansion microscopy. *J. Heat Transfer* **120,** 297–305 (1998).
7. Cannaerts, M., Buntinx, D., Volodin, A. & Van Haesendonck, C. Calibration of a scanning Joule expansion microscope (SJEM). *Appl. Phys. A* **72,** S67–S70 (2001).
8. Gurrum, S. P., King, W. P., Joshi, Y. K. & Ramakrishna, K. Size effect on the thermal conductivity of thin metallic films investigated by scanning Joule expansion microscopy. *J. Heat Transfer* **130,** 082403 (2008).
9. Pop, E. Energy dissipation and transport in nanoscale devices. *Nano Res.* **3,** 147–169 (2010).
10. Dorgan, V. E., Bae, M-H. & Pop, E. Mobility and saturation velocity in graphene on SiO_2. *Appl. Phys. Lett.* **97,** 082112 (2010).
11. Bae, M-H., Ong, Z-Y., Estrada, D. & Pop, E. Imaging, simulation, and electrostatic control of power dissipation in graphene devices. *Nano Lett.* **10,** 4787–4793 (2010).
12. Jackson, R. & Graham, S. Specific contact resistance at metal/carbon nanotube interfaces. *Appl. Phys. Lett.* **94,** 012109 (2009).
13. Lan, C. *et al.* Measurement of metal/carbon nanotube contact resistance by adjusting contact length using laser ablation. *Nanotechnology* **19,** 125703 (2008).
14. Franklin, A. D. & Chen, Z. Length scaling of carbon nanotube transistors. *Nature Nanotech.* **5,** 858–862 (2010).
15. Schroder, D. K. *Semiconductor Material and Device Characterization* (Wiley, 2006).
16. Chieh, Y. S., Perera, A. K. & Krusius, J. P. Series resistance of silicided ohmic contacts for nanoelectronics. *IEEE Trans. Electron. Dev.* **39,** 1882–1888 (1992).
17. DiSalvo, F. J. Thermoelectric cooling and power generation. *Science* **285,** 703–706 (1999).
18. Schroder, D. K. & Babcock, J. A. Negative bias temperature instability: road to cross in deep submicron silicon semiconductor manufacturing. *J. Appl. Phys.* **94,** 1–18 (2003).
19. Freitag, M., Chiu, H-Y., Steiner, M., Perebeinos, V. & Avouris, P. Thermal infrared emission from biased graphene. *Nature Nanotech.* **5,** 497–501 (2010).
20. Xu, X., Gabor, N. M., Alden, J. S., van der Zande, A. M. & McEuen, P. L. Photo-thermoelectric effect at a graphene interface junction. *Nano Lett.* **10,** 562–566 (2009).
21. Wei, P., Bao, W., Pu, Y., Lau, C. N. & Shi, J. Anomalous thermoelectric transport of Dirac particles in graphene. *Phys. Rev. Lett.* **102,** 166808 (2009).
22. Zuev, Y. M., Chang, W. & Kim, P. Thermoelectric and magnetothermoelectric transport measurements of graphene. *Phys. Rev. Lett.* **102,** 096807 (2009).
23. Checkelsky, J. G. & Ong, N. P. Thermopower and Nernst effect in graphene in a magnetic field. *Phys. Rev. B* **80,** 081413 (2009).
24. Zhu, W., Perebeinos, V., Freitag, M. & Avouris, P. Carrier scattering, mobilities, and electrostatic potential in monolayer, bilayer, and trilayer graphene. *Phys. Rev. B* **80,** 235402 (2009).
25. International Technology Roadmap for Semiconductors (ITRS), http://public.itrs.net (2009).
26. Thompson, S. E. *et al.* In search of 'Forever,' continued transistor scaling one new material at a time. *IEEE Trans. Semicond. Manuf.* **18,** 26–36 (2005).
27. Ishigami, M., Chen, J. H., Cullen, W. G., Fuhrer, M. S. & Williams, E. D. Atomic structure of graphene on SiO_2. *Nano Lett.* **7,** 1643–1648 (2007).
28. Koh, Y. H., Bae, M.-H., Cahill, D. G. & Pop, E. Reliably counting atomic planes of few-layer graphene ($n > 4$). *ACS Nano* **5,** 269–274 (2011).
29. Malard, L. M., Pimenta, M. A., Dresselhaus, G. & Dresselhaus, M. S. Raman spectroscopy in graphene. *Phys. Rep.* **473,** 51–87 (2009).
30. Silvestrov, P. G. & Efetov, K. B. Charge accumulation at the boundaries of a graphene strip induced by a gate voltage: electrostatic approach. *Phys. Rev. B* **77,** 155436 (2008).
31. Vasko, F. T. & Zozoulenko, I. V. Conductivity of a graphene strip: width and gate-voltage dependencies. *Appl. Phys. Lett.* **97,** 092115 (2010).

Acknowledgements

This work was supported by the Air Force Office of Scientific Research MURI FA9550-08-1-0407, Office of Naval Research grants N00014-07-1-0767, N00014-09-1-0180 and N00014-10-1-0061, and the Air Force Young Investigator Program (E.P.).

Author contributions

K.L.G. performed measurements and simulations. M-H.B. fabricated devices and assisted with simulations. E.P. implemented the computational model and physical interpretation, with help from F.L., while E.P. and W.P.K. conceived the experiments. All authors discussed the results. K.L.G., E.P. and W.P.K. co-wrote the manuscript.

Additional information

The authors declare no competing financial interests. Supplementary information accompanies this paper at www.nature.com/naturenanotechnology. Reprints and permission information is available online at http://npg.nature.com/reprintsandpermissions/. Correspondence and requests for materials should be addressed to E.P. and W.P.K.

nature nanotechnology

SUPPLEMENTARY INFORMATION

DOI: 10.1038/NNANO.2011.39

Nanoscale Joule heating, Peltier cooling and current crowding at graphene-metal contacts

Kyle L. Grosse,[1,2] Myung-Ho Bae,[2,3] Feifei Lian,[2,3] Eric Pop,[2,3,4,*] and William P. King[1,2,4,5,*]

[1]*Department of Mechanical Science and Engineering*

[2]*Micro and Nano Technology Laboratory*

[3]*Department of Electrical and Computer Engineering*

[4]*Beckman Institute for Advanced Studies*

[5]*Department of Materials Science and Engineering*

University of Illinois Urbana-Champaign, Urbana IL USA 61801

Table of Contents:

*Contact: epop@illinois.edu, wpk@illinois.edu

DOI: 10.1038/NNANO.2011.39

1. Graphene Device Characterization

Raman spectroscopy and two-probe electrical measurements were used to characterize the graphene transistors used in this study. Figures S1(a) and (b) show the single Lorentzian fit to the 2D peak of the Raman measurement for length L = 5 μm and width W = 4 and 6 μm graphene devices (633 nm, 1.7 mW laser). The 2D peak shift of ~2650 cm^{-1} and full width at half maximum (fwhm) of 31.6 and 28.9 cm^{-1} for the two devices is consistent with other studies for monolayer graphene.[1-3] Electronic measurements are shown in the inset of Fig. 2(b) (W = 4 μm) and Fig. S5(b) (W = 6 μm) with graphene resistance R as a function of gate voltage V_G. The neutral (Dirac) voltage for the W = 4 and 6 μm samples was measured as V_0 = 32 and 28 V, respectively. Determination of carrier mobility and carrier puddle density is explained below.

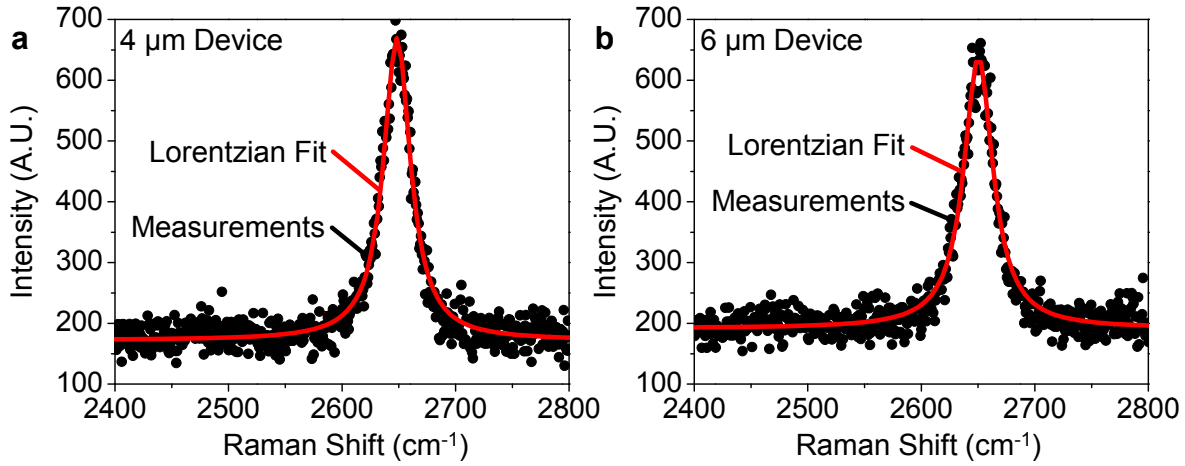

Figure S1 | Raman spectroscopy. *2D Raman peaks for two graphene devices used in this work (length L = 5 μm, width W = 4 and 6 μm). Single Lorentzian fit confirms monolayer graphene.*[1-3]

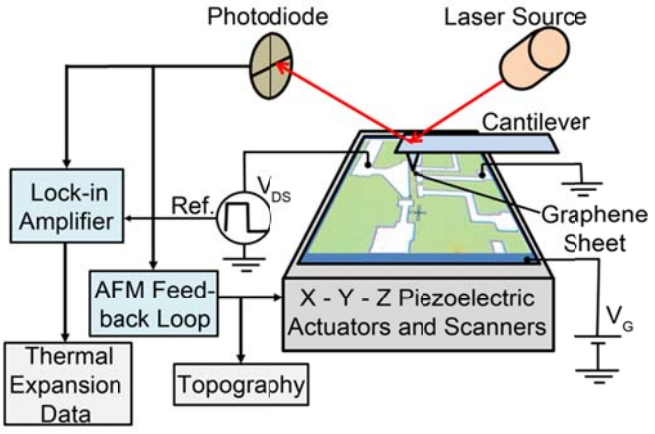

Figure S2 | Experimental Setup. *An atomic force microscope (AFM) feed-back loop monitors cantilever deflections using a laser-photodiode system and by operating a piezoelectric stage. The sample experiences periodic thermo-mechanical expansions due to Joule heating from a periodic waveform supplied to the sample. A lock-in amplifier technique is used to record the thermo-mechanical expansion. The back-gate voltage V_G is applied to the Si substrate and controlled using a constant voltage source that shares a common ground with the source electrode.*

2. Nanometer-Scale Temperature Measurements

Back-gated Scanning Joule Expansion Microscopy (SJEM). Figure S2 shows the experimental set-up for back-gated SJEM.[4-6] A square wave at 65 kHz, 50% duty, with amplitude V_{DS} induces Joule heating within the device. The temperature increases within the device, the PMMA, and the substrate, which in turn causes thermo-mechanical expansion of the device, PMMA, and substrate. This expansion is measured by an AFM tip in contact with the top surface of the PMMA. A lock-in amplifier with an equivalent noise bandwidth of ~100 Hz records the cantilever deflection at this frequency. The unipolar waveform allows measurement of forward and reverse bias heating. A constant voltage is supplied to the back-gate during all experiments.

Correlating Temperature Rise to Measured Thermo-mechanical Expansions The measured sample expansion can be related to the temperature rise of the device. Previous publications by us and others describe the details of heat flow from the device into the nearby substrate and polymer film, the resulting temperature distributions and thermomechanical displacements, and how the measured displacements can be translated into temperature rise.[4-6] Our approach is based on these previous publications and a deeper analysis is available therein.

The observed thermomechanical displacements can be related to device temperature through a proportionality constant that is obtained by modeling the heat flow within the sample. This is the approach developed in our previous work on measuring nanometer-scale temperature distributions in interconnects.[4] A one-dimensional simulation models out-of-plane heat flow using the transient heat diffusion equation with constant coefficients and uses an implicit solution method. The one-dimensional model is used as the sample is much wider than it is thick, and the temperature gradient in the z-direction is much larger than the temperature gradient in the lateral directions. The layer materials and thicknesses in the simulation are selected to match those from the experiment, and the layer properties are as shown in Table S1. The simulation input is a periodic heat generation within the device, and the output is the temperature distribution in the *z*-direction. The temperature-dependent thermomechanical expansion is then calculated in the z-direction for each element by taking the product of the element length, temperature rise, and linear thermal expansion coefficient. By summing the expansion of each element, the simulation calculates the sample expansion L. Because of the mechanical boundary conditions, the expansion is mainly in the *z*-direction. This processes is repeated for each time step, t. The model runs for 100 heating cycles to ensure it is at steady state. At steady-state the amplitude of sample expansion and temperature rise of the heating element is found by $\Delta L_{ss} = max(L_{SS}) - min(L_{SS})$ and $\Delta T_{ss} = max(T_{SS}) - min(T_{SS})$ where the subscript SS denotes time steps contained in the steady-state period. The ratio of ΔT_{ss} to ΔL_{ss} yields the proportionality constant that relates the measured expansion to graphene temperature.

Figure S3 shows sample thickness across the sample, which is slightly different at the electrodes compared to at the graphene sheet and thus the simulation is run separately for each of these regions. The model for the graphene sheet is composed of 65 nm of PMMA, 300 nm of SiO_2, and 15 μm of Si. The model composition changes at the electrodes to 55 nm of PMMA, 40 nm of Pd, 300 nm of SiO_2, and 15 μm of Si. The model is bound by a constant temperature at the Si base and an adiabatic PMMA surface. The finite element immediately above the SiO_2 layer experiences heat generation from a square wave at 65 kHz with 50% duty with a heat generation of 10^{15} Wm^{-3}. The model resolution was set with an element size of 5 nm and a time step of ~150 ns. The thermo-physical properties used in the model are listed in Table S1. The Wiedemann-Franz law is used to calculate the conductivity of Pd from a value of electrical resistivity found

DOI: 10.1038/NNANO.2011.39

below. Note the Si substrate is highly n-type doped, with reduced thermal conductivity compared to bulk value. The model calculates ΔT_{ss} / ΔL_{ss} to be a constant 61.7 Knm^{-1} and 59.2 Knm^{-1} for the electrode and graphene sheet models. More details of the heat transfer and thermomechanical expansion model can be found in our previous publication.[4]

Table S1 | *Thermophysical properties of materials used in simulations.*

Material	Thermal Conductivity ($Wm^{-1}K^{-1}$) [7, 8]	Thermal Diffusivity $\cdot 10^6$ (m^2s^{-1})	Coefficient of Thermal Expansion (K^{-1})
PMMA	0.18	0.1	100
Pd	42	14.3	11.8
SiO_2	1.3	0.79	0.5
Si	40	24	2.6

Temperature Measurement Resolution. The measurement resolution can be considered in terms of the temperature resolution and the spatial resolution, and both have been thoroughly described in previous publications.[4-6]

The spatial resolution of the AFM measurement is ~1 nm in our Asylum MFP-3D AFM, limited by the quality of the AFM scanner and the sharpness of the tip. The spatial resolution of the temperature measurement is thus not limited by the AFM setup but rather heat flow in the sample. The heat generated within the sample flows in the *x*, *y*, and *z* directions, such that there is heat spreading in the sample and the polymer film. However, the majority of the heat flow is in the *z*-direction as the temperature gradient in this direction is much larger than in the *x* or *y* directions, thus the temperature distribution in the polymer film is spread by a width that is smaller than the film thickness. The thermomechanical expansion of the polymer, and underlying Si, is linear with temperature rise, such that the measured thermomechanical expansion is largest above the hotspot in the sample. Therefore the majority of the thermomechanical expansion is in the *z*-direction rather than in the lateral directions.

Given a 90% confidence interval of the average standard deviation of the measurements, our measurement resolution is ~250 mK and ~10 nm. We found that this resolution can be improved by extending scan time, but this was limited here as the Dirac voltage could shift during scans, distorting the temperature profiles. Higher gate voltages exacerbated this problem as well, limiting measurements to $V_G < 25$ V. The signal to noise ratio was improved by averaging 128 line scans (each 3 μm long) to create each temperature profile. The temperature resolution of the technique was found constant for the 0-20 K temperature rise in this study. Thus, the relative precision of SJEM is seen to increase with the temperature rise.

Temperature Measurement Error Analysis. Accuracy of the temperature measurement is limited by two effects: uncertainty in ellipsometer measurements and uncertainty in cantilever sensitivity. The PMMA thickness measured by ellipsometry deviates by ± 2 nm introducing ~± 2% uncertainty into measurements. The uncertainty in the cantilever sensitivity was ± 5%, which introduces ±1 K uncertainty for a 20 K temperature rise, and proportionally less otherwise. Decreasing the uncertainty in cantilever sensitivity and sample composition will increase the accuracy of AFM temperature measurements.

The thickness of the PMMA changes slightly in the vicinity of the graphene-Pd boundary, which leads to additional uncertainty. AFM topography of the sample with and without the PMMA coat show the PMMA thickness t_{PMMA} can vary by 5 - 10 nm at the graphene-Pd interface. As the model assumes t_{PMMA} is uniform over the graphene and electrode, error is introduced at these locations. The error is recorded as the difference in ΔT_{ss} / ΔL_{ss} for the sample with the measured t_{PMMA} and the assuming t_{PMMA} = 55 or 65 nm from above, and divided by the former. As shown in Fig. S3b, this error is at most 5% due to the non-conformal PMMA coverage. Thus this error is not large. However, error may be introduced at this location due to lateral heat flow as the temperature gradient in *x* becomes comparable to the gradient in *z*, but more complex models are required to evaluate this.

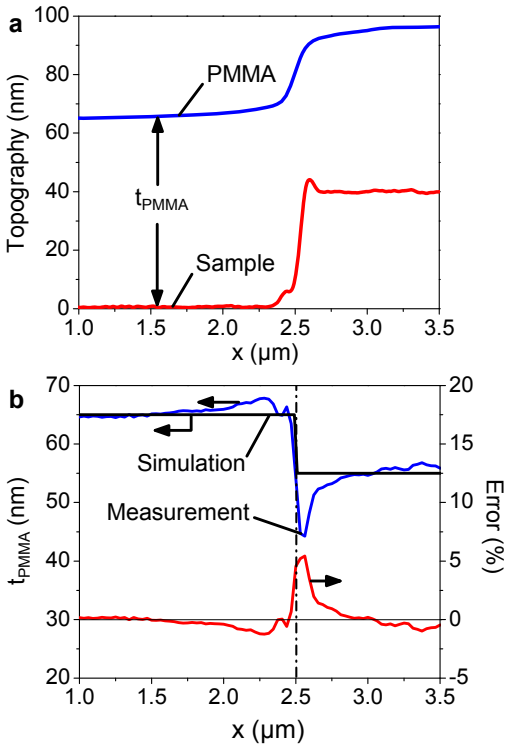

Figure S3 | Variation in PMMA thickness. *(a) AFM Topography of the graphene-Pd boundary with and without the PMMA coating. The difference in shape of the two curves indicates the PMMA thickness (t_{PMMA}) varies across the sample. The PMMA topography is vertically offset 65 nm, consistent with ellipsometer measurements. (b) Comparison of measured t_{PMMA} to the t_{PMMA} used in simulations (top lines). The difference between the two is quantified as the error in the predicted temperature with the measured t_{PMMA} to the t_{PMMA} used in simulation (bottom line). A positive value indicates where temperature predictions may underestimate graphene temperature. The maximum error is 10% percent over a ~100 nm distance and is otherwise within ± 2%. The assumption of uniform t_{PMMA} over the electrode and graphene is shown as appropriate. The graphene-Pd boundary is shown at x = 2.5 μm.*

DOI: 10.1038/NNANO.2011.39

3. Addition of Contact Effects to Graphene Model

Current crowding (CC) and thermoelectric (TE) effects were added to our existing model of graphene devices already including the Joule heating, electrostatic, and current-continuity equations.[2] CC leads to a potential drop along the graphene-metal contact,[9]

$$V_x = \frac{I_D}{W}\left(R_S \rho_C\right)^{1/2} \frac{\cosh(x/L_T)}{\sinh(L_C/L_T)} \qquad \text{(E1)}$$

where x is the horizontal distance from the graphene-metal edge and symbols are as defined in the main text. We note the sheet resistance $R_S = 1/[q(n + p)\mu]$ is computed consistently with the charge density at each point along the graphene under the contact. The electric field along the contact is $F_x = -\mathrm{d}V/\mathrm{d}x$. The CC heating term along the metal-graphene contact is $P_{CC} = I_D \cdot F_x$ per unit length (W/m), which is numerically included into the heat equation.[2]

The thermoelectric (TE) effect at the contacts is driven by a power generation term $P_{TE} = \pm W S_x T_x V_x / \rho_C$ per unit length (W/m), which can be either positive or negative depending on the direction of current flow (+ for current into contact, - for current out). Here we neglect the thermopower of the metal contact itself, which is ~4 μV/K for Pd and much smaller than the thermopower of graphene. The thermopower (Seebeck coefficient) of graphene is derived from the semi-classical Mott relationship[10] (we note a missing square root term in Ref. [10]) following the definitions of charge density and Fermi level consistent with our recent work.[2, 8] This results in a closed-form approximation for the graphene thermopower:

$$S_x = -\frac{2\pi^{3/2} k_B^2 T^*}{3q\hbar v_F} \frac{(n-p)\sqrt{|n-p|}}{(n+p)^2} \qquad \text{(E2)}$$

where the temperature T_x, the electron n_x and hole density p_x vary with position x along the metal-graphene contact, consistent with the model in Ref. [8]. We note that in order to match the experimental data of Ref. [11], we use $T^* = cT$ where $c = 0.7$, as shown by fitting in Fig. S4.

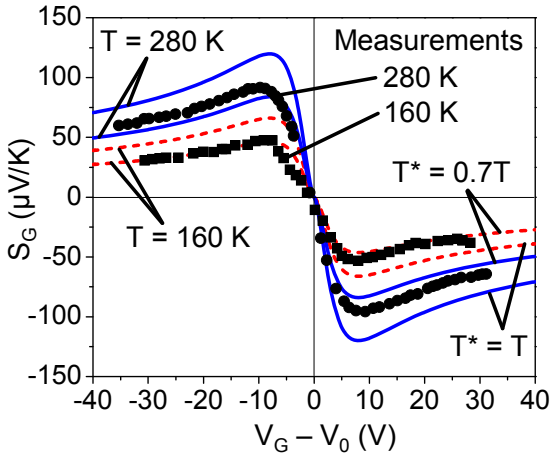

Figure S4 | Seebeck model. *Comparison of simple Seebeck model (lines) from Eq. (E2) with experimental data by Checkelsky et al (points).[11] We find that T* = cT where c = 0.7 provides an excellent fit to the experimental thermopower.*

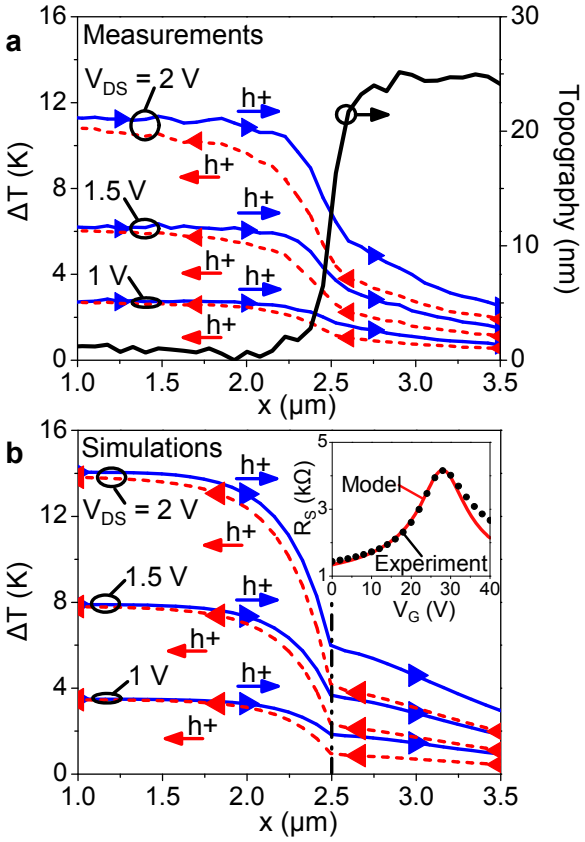

Figure S5 | Contact heating and cooling of a second device. *(a) Measured and (b) predicted temperature profile near the graphene-metal contact for a second device with W = 6 μm. Operating conditions are V_G = 0 V for both forward and reverse V_{DS} = 1, 1.5, and 2 V. The edge of the graphene-Pd contact is at 2.5 μm. The inset shows the graphene resistance (R) including contacts vs. gate voltage (V_G) for both experiment (symbols) and simulation fit (line). Dirac voltage is V_0 = 28 V. Also compare with Fig. 2 in main text.*

4. Fitting Simulations to Data

Electrical. Fitting the model to the measured R vs. V_G in the insets of Fig. 2(b) (W = 4 μm) and Fig. S5(b) (W = 6 μm) yields the mobility μ, carrier puddle density n_0, and series resistance R_{series} of the two-terminal graphene devices. The best fit between the model and measurements was obtained with R_{series} = 650 Ω and 575 Ω for the W = 4 and 6 μm wide devices, respectively, corresponding to a resistivity ρ_{Pd} = 17 μΩ·cm for the Pd lines connecting the device pads to the outside measurement equipment. In addition, we found the best-fit mobility and carrier puddle density, $\mu \approx 3230$ cm^2/V·s and $n_0 \approx 1.8\times10^{11}$ cm^{-2} for the 4 μm wide device, and $\mu \approx 4000$ cm^2/V·s and $n_0 \approx 1.2\times10^{11}$ cm^{-2} for the 6 μm wide device, similar to other studies.[2, 12, 13]

Thermal. Once μ and n_0 are known, only the graphene-Pd contact resistivity ρ_C is required to fit predicted and measured temperature profiles in Fig. 2 and Fig. S5. For the W = 4 and 6 μm devices, we find $\rho_C \approx 150$ and 200 Ω·μm^2 respectively. The thermal conductivities[8, 14] used

DOI: 10.1038/NNANO.2011.39

in the model are listed in Table 1. The thermal conductivity[14] of 600 $Wm^{-1}K^{-1}$ was used for graphene with an additional (65/0.34)×0.18 ≈ 35 $Wm^{-1}K^{-1}$ to simulate lateral heat spreading due to the 65 nm of PMMA on top, although the model is relatively insensitive to this correction.

5. Analysis of 6 μm Wide Device

Figure S5 compares measured temperature profiles (a) with predictions (b) for a secondary device with W = 6 μm. The analysis of the 6 μm width device is similar to the 4 μm device in the main text and many duplicate details are omitted here. We set V_G = 0 V for the predictions and measurements shown in Fig. S5, which corresponds to a hole concentration of $p \approx 2.0\times 10^{12}$ cm^{-2} as V_0 = 28 V. The predicted temperature profiles use the (JH+CC+TE) model, which agrees well with experimental observations.

Figure S6(a) shows how JH, CC, and TE effects change the temperature profile of the 6 μm wide device at the graphene-Pd contact for V_{DS} = 1 V. JH is the dominant effect in the graphene itself, as the addition of CC and TE have little change there. However, the addition of CC to JH introduces an additional heat source in the electrode, leading to a more gradual temperature decrease there. CC also introduces the effective current transfer length L_T which varies from 520 to 225 nm in the 6 μm wide device, as V_G changes from 0 to V_0 = 28 V. The addition of the TE effect to the "JH+CC" model introduces electrode heating and cooling with carrier flow, which is evident in the measured temperature profiles. Similar to the 4 μm device (main text), the heating and cooling are better understood when examining the difference between the forward and reverse biased temperature profiles, as in Fig. S6(b). In the 6 μm wide device the TE effect cools and heats the electrode by ~0.5 K (~30 %). Similar to the 4 μm wide device, ΔT_{ASM} is a function of V_G, plotted in Fig. S6(c) with experimental measurements at V_{DS} = 1 V.

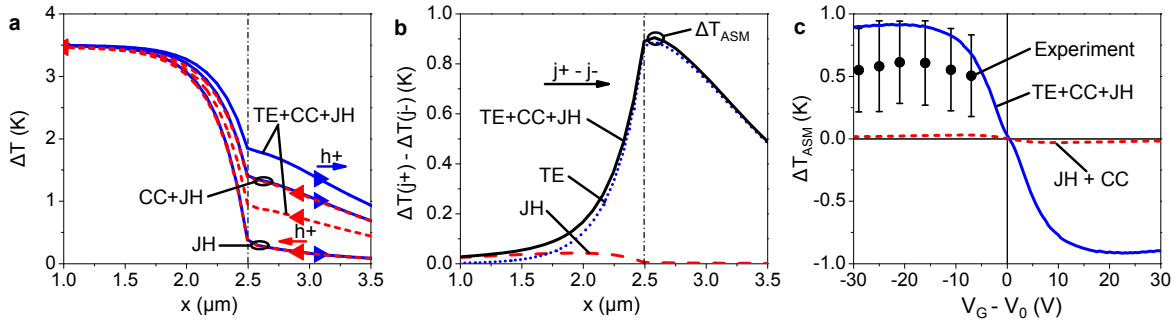

Figure S6 | Relative contribution of contact effects for a secondary device (W = 6 μm). *(a) Simulations showing relative contributions of JH, CC, and TE to the temperature distribution at the graphene-Pd contact at V_{DS} = 1 V and V_G = 0 V. Also see Fig 3 of main text. All three components (TE+CC+JH) are necessary to match the experimental data. (b) Electrode heating and cooling is quantified by taking the difference between temperature under forward and reverse current flow. The maximum temperature difference between the two biases is defined as ΔT_{ASM}. (c) Comparison of measured and predicted ΔT_{ASM} as a function of V_G relative to V_0, with JH, CC, and TE contributions to the predicted ΔT_{ASM} shown. Also see Fig. 4 of main text.*

6. Extracting the Seebeck Coefficient of Graphene

Although in the numerical calculations we use the analytical expression for the Seebeck coefficient (thermopower) of graphene as in equation (E2), this Seebeck coefficient can also be extracted from direct comparison of the model with our contact temperature measurements. In other words, S_G can be obtained from Fig. 4(a) and Fig. S6(c) by fitting the predicted ΔT_{ASM} to the measured ΔT_{ASM}. The upper and lower limits are found by adjusting ΔT_{ASM} until the predicted ΔT_{ASM} is out of range of the measurement error bars. The fit of this model is shown in Fig. S7, finding that S_G ranges from 27 to 62 μV/K, with the best fit at ~41 μV/K for the 6 μm device and for the 4 μm device S_G ranges from 41 to 82 μV/K, with the best fit at ~63 μV/K at $V_G - V_0 = -25$ V at 300 K. Across the two devices S_G is found to be approximately 52 μV/K, consistent with previous studies.[10, 11]

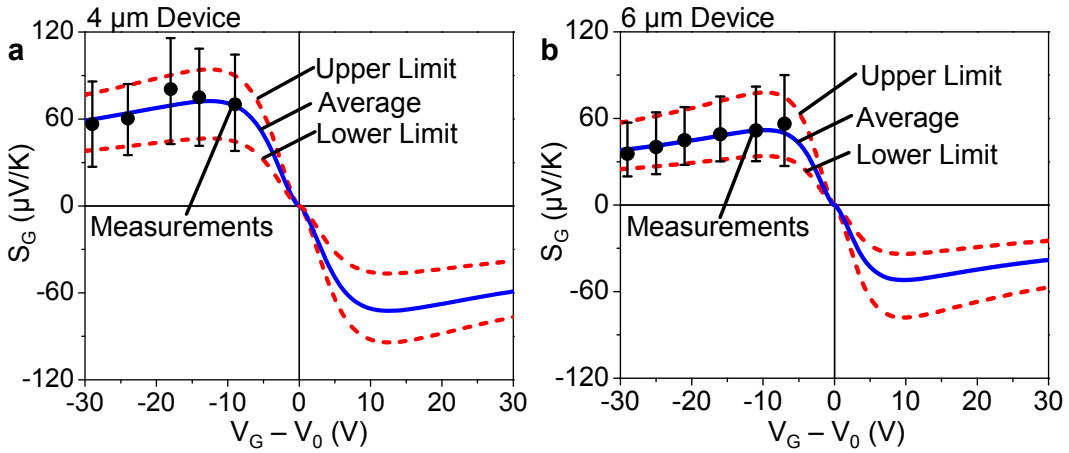

Figure S7 | Seebeck coefficient. *Extracted Seebeck coefficient at 300 K from the experiment shown with measurements for the 4 μm (a) and 6 μm (b) wide device. The upper and lower limits correspond to fitting the deviation of the measurements at 90% confidence.*

7. Movie File: Effect of Back-gate on Contact Heating and Cooling

The supplementary movie file details the transition of TE dominated ΔT_{ASM} to JH effects as a function of V_G relative to V_0 at the graphene-Pd contact by taking the difference between the temperature profile under forward and reverse bias. The movie is similar to Fig. S6(b) with the position of ΔT_{ASM} defined by the vertical dashed line. The model parameters are similar to the 6 μm device with $\rho_C = 200\ \Omega{\cdot}\mu m^2$, $\mu = 4000\ cm^2/V{\cdot}s$ and $V_{DS} = 2$ V. As V_G - V_0 approaches zero two events occur: (1) JH hot spot effects become large at the electrode[2] and (2) the Seebeck coefficient decreases, lowering TE effects.[10, 11, 15] After V_G - $V_0 = 0$ V the majority carrier switches to electrons which reverses carrier flow, hot spot,[2, 16] and the TE effect,[10, 11, 15, 17] although the definition of current flow remains the same. As $V_G - V_0$ increases, the TE effect increases, hot spot effects decrease, and the curves become similar to their initial states.

DOI: 10.1038/NNANO.2011.39

Supplementary References:

1. Ferrari, A.C. et al. Raman Spectrum of Graphene and Graphene Layers. *Physical Review Letters* **97**, 187401 (2006).
2. Bae, M.-H., Ong, Z.-Y., Estrada, D. & Pop, E. Imaging, Simulation, and Electrostatic Control of Power Dissipation in Graphene Devices. *Nano Letters* **10**, 4787-4793 (2010).
3. Abdula, D., Ozel, T., Kang, K., Cahill, D.G. & Shim, M. Environment-Induced Effects on the Temperature Dependence of Raman Spectra of Single-Layer Graphene. *The Journal of Physical Chemistry C* **112**, 20131-20134 (2008).
4. Gurrum, S.P., King, W.P., Joshi, Y.K. & Ramakrishna, K. Size Effect on the Thermal Conductivity of Thin Metallic Films Investigated by Scanning Joule Expansion Microscopy. *Journal of Heat Transfer* **130**, 082403-082408 (2008).
5. Majumdar, A. & Varesi, J. Nanoscale Temperature Distributions Measured by Scanning Joule Expansion Microscopy. *Journal of Heat Transfer* **120**, 297-305 (1998).
6. Varesi, J. & Majumdar, A. Scanning Joule expansion microscopy at nanometer scales. *Applied Physics Letters* **72**, 37-39 (1998).
7. Assael, M., Botsios, S., Gialou, K. & Metaxa, I. Thermal Conductivity of Polymethyl Methacrylate (PMMA) and Borosilicate Crown Glass BK7. *International Journal of Thermophysics* **26**, 1595-1605 (2005).
8. Dorgan, V.E., Bae, M.-H. & Pop, E. Mobility and saturation velocity in graphene on SiO_2. *Applied Physics Letters* **97**, 082112-082113 (2010).
9. Schroder, D.K. Semiconductor Material and Device Characterization. (Wiley Interscience, 2006).
10. Zuev, Y.M., Chang, W. & Kim, P. Thermoelectric and Magnetothermoelectric Transport Measurements of Graphene. *Physical Review Letters* **102**, 096807 (2009).
11. Checkelsky, J.G. & Ong, N.P. Thermopower and Nernst effect in graphene in a magnetic field. *Physical Review B* **80**, 081413 (2009).
12. Martin, J. et al. Observation of electron-hole puddles in graphene using a scanning single-electron transistor. *Nat Phys* **4**, 144-148 (2008).
13. Kim, S. et al. Realization of a high mobility dual-gated graphene field-effect transistor with Al_2O_3 dielectric. *Applied Physics Letters* **94**, 062107-062103 (2009).
14. Seol, J.H. et al. Two-Dimensional Phonon Transport in Supported Graphene. *Science* **328**, 213-216 (2010).
15. Wei, P., Bao, W., Pu, Y., Lau, C.N. & Shi, J. Anomalous Thermoelectric Transport of Dirac Particles in Graphene. *Physical Review Letters* **102**, 166808 (2009).
16. Freitag, M., Chiu, H.-Y., Steiner, M., Perebeinos, V. & Avouris, P. Thermal infrared emission from biased graphene. *Nat Nano* **5**, 497-501 (2010).
17. Xu, X., Gabor, N.M., Alden, J.S., van der Zande, A.M. & McEuen, P.L. Photo-Thermoelectric Effect at a Graphene Interface Junction. *Nano Letters* **10**, 562-566 (2009).